Stabilizing Multi-Electron NASICON-Na$_{1.5}$V$_{0.5}$Nb$_{1.5}$(PO$_4$)$_3$ Anode via Structural Modulation for Long-Life Sodium-Ion Batteries

Biplab Patra, Rashmi Hegde, Anirudh Natarajan, Debolina Deb, Dorothy Sachdeva, Narayanan Ravishankar, Keshav Kumar, Gopalakrishnan Sai Gautam, and Premkumar Senguttuvan*

Multi-electron NAtrium SuperIonic CONductor (NASICON)-Nb$_2$(PO$_4$)$_3$ (N$_0$NbP) is an attractive Na-ion battery anode, owing to its low intercalation voltage (1.4 V vs Na$^+$/Na^0) and high capacity ($\approx$150 mAh g^{-1}). However, it suffers from poor capacity retention due to structural degradation. To overcome this issue, extra Na$^+$ ions are introduced at the Na(1) sites, via V^{3+} substitution, which can act as stabilizing agents to hold lantern units together during cycling, producing NASICON-Na$_{1.5}$V$_{0.5}$Nb$_{1.5}$(PO$_4$)$_3$ (N$_{1.5}$VNbP). The N$_{1.5}$VNbP anode exhibits reversible capacities of $\approx$140 mAh g^{-1} at 1.4 V versus Na$^+$/Na^0 through Nb^{5+}/Nb^{4+}/Nb^{3+} and V^{3+}/V^{2+} redox activities. The extra Na$^+$ ions in the framework forms a complete solid-solution during Na (de)intercalation and enhances sodium diffusivity, in agreement with first-principles calculations. Further, N$_{1.5}$VNbP demonstrates extraordinary cycling (89% capacity retention at 5C after 500 cycles) and rate performances (105 mAh g^{-1} at 5C). Upon pairing the N$_{1.5}$VNbP anode with the NASICON-Na$_3$V$_2$(PO$_4$)$_3$ cathode, the full Na-ion cell delivers a remarkable energy density of 98 Wh kg^{-1} (based on the mass of anode and cathode) and retains 80% of its capacity at 5C rate over 1000 cycles. The study opens new possibilities for enhancing the electrochemical performance of NASICON anodes via chemical and structural modulations.

1. Introduction

Low-cost, safe, and ultra-long-life rechargeable batteries are pre-requisites for the electrification of transportation and large-scale grid storage. While modern Li-ion technology has been seriously pursued for the former application, the scarcity and uneven geographical distribution of Li and Co resources limit their grid storage utility.[1] From this viewpoint, chemically analogous sodium-ion batteries (SIBs) are considered the frontrunner for low-cost and large-scale energy storage applications due to the earth-abundance of sodium.[2–6] More significantly, the design knowledge gained from Li-ion materials can be successfully imparted to develop SIBs, which has accelerated not only the materials discovery but also aided in developing viable SIB prototypes. While various classes of Na-ion cathode materials have been developed, the research on anode is centered around intercalation, alloy, and conversion type reactions, similar to Li-ion batteries.[7,8] The last two classes of materials offer high gravimetric capacities (400–1200 mAh g^{-1}) due to multi-electron exchange during cycling. However, they undergo several phase changes involving chemical bond breaking and forming along with repeated destruction and reconstruction of the solid electrolyte interphase (SEI) and consumption of electrolytes, which

B. Patra, R. Hegde, K. Kumar, P. Senguttuvan
New Chemistry Unit, International Centre for Materials Science, and School of Advanced Materials
Jawaharlal Nehru Centre for Advanced Scientific Research
Jakkur, Bengaluru, Karnataka 560064, India
E-mail: prem@jncasr.ac.in

A. Natarajan, D. Deb, G. S. Gautam
Department of Materials Engineering
Indian Institute of Science
Bengaluru, Karnataka 560012, India

A. Natarajan
Department of Metallurgical and Materials Engineering
National Institute of Technology
Tiruchirappalli, Tamil Nadu 620015, India

D. Sachdeva, N. Ravishankar
Materials Research Centre
Indian Institute of Science
Bengaluru, Karnataka 560012, India

ADVANCED
SCIENCE NEWS

www.advancedsciencenews.com

ADVANCED
ENERGY
MATERIALS

www.advenergymat.de

ultimately results in poor capacity retention.[9,10] On the contrary, intercalation-based hard carbon anode delivers reversible capacities of 200–350 mAh g^{-1} at a relatively lower voltage (<0.1 V vs Na$^+$/Na^0) and low volumetric energy density for a few hundred cycles.[11,12] While the rate performance of hard carbon anodes still needs improvement, they can exhibit Na metal plating under high current densities which can cause serious safety issues. Further, Ti-based oxide intercalation anodes display moderate storage capacities (100–170 mAh g^{-1}) but suffer from cycling instabilities mostly due to an unstable SEI.[13,14]

Alternatively, polyanionic materials,[15,16] particularly sodium superionic conductor (NASICON)-type frameworks have been explored as possible Na-ion anodes. NaTi$_2$(PO$_4$)$_3$ (NTP) delivers reversible capacities of ≈100 mAh g^{-1} at 2.1 V versus Na$^+$/Na^0, according to the reaction, $NaTi_2(PO_4)_3 + 2\ Na^+ + 2\ e^- \leftrightarrow Na_3Ti_2(PO_4)_3$.[17,18] Although several reports demonstrated stable cycling performances and rate capacities for NTP anode with carbon-coating and particle nano-sizing, the higher insertion voltage and moderate storage capacity eventually reduce the energy density for practical application.[19–21] Similarly, Na$_3$V$_2$(PO$_4$)$_3$ (NVP) anode is also limited by its low storage capacity (≈50 mAh g^{-1}) despite its lower insertion voltage (≈1.6 V) compared to the NTP anode (≈2.1 V).[22–24] To overcome the challenges associated with NASICON anodes, we recently tailored an "empty" NASICON-Nb$_2$(PO$_4$)$_3$ (N$_0$NbP) anode which undergoes multi-electron transfer to deliver higher reversible capacities (≈150 mAh g^{-1}) at a low average voltage (≈1.4 V).[25] However, its application in practical SIBs is hampered due to its limited cycling stability and poor rate performance due to structural instability (detailed in the later sections). One way to mitigate the structural instability of N$_0$NbP and thereby improve its electrochemical performance is via structural/chemical modulation, which is the main focus of this work.

Herein, we unveil a chemical substitution strategy, namely aliovalent substitution of Nb$^{5+/4+}$ with V^{3+}, to overcome the structural instability of the N$_0$NbP anode. Specifically, the aliovalent substitution introduces additional sodium ions at the Na(1) site of the NASICON framework, resulting in an anode of composition Na$_{1.5}$V$_{0.5}$Nb$_{1.5}$(PO$_4$)$_3$ (or N$_{1.5}$VNbP). Using combined X-ray diffraction (XRD), X-ray absorption spectroscopy (XAS), and electrochemical measurements, we show the incorporation of additional sodium ions via chemical substitution improves structural and cycling stabilities and Na (de)intercalation kinetics of the NASICON host. Additionally, we have performed density functional theory (DFT)[26,27] based calculations to understand the phase behavior of the N$_{1.5}$VNbP anode with Na exchange. We have performed a systematic screening on the compatibility of Na-ion electrolytes with the N$_{1.5}$VNbP anode to optimize its cycling and rate performances. Our combined structural and electrolyte modulations yield excellent capacity retention (89% after 500 cycles) and rate capability of the N$_{1.5}$VNbP anode upon pairing with glyme-based electrolytes. Finally, a full Na-ion cell comprising NVP as cathode and N$_{1.5}$VNbP as anode is demonstrated with the highest average voltage of (≈1.9 V) compared to the known NASICON-based cells.[19,28–31]

2. Results and Discussion

Initially, we assess the electrochemical performance of N$_0$NbP anode against sodium metal across two different voltage windows (i.e., 3.0–1.1 V and 3.0–1.0 V vs Na$^+$/Na^0) at C/2 rate using 0.7 M NaBF$_4$/diglyme as the electrolyte. The details of synthesis, structural, and morphological characterization of N$_0$NbP anode are presented in the experimental section and the supporting information (see Figure S1, Supporting Information).[25] The voltage versus capacity and dQ/dV profiles of N$_0$NbP are displayed in **Figure 1**a–d. Upon cycling in the 3.0–1.1 V versus Na$^+$/Na^0 window, the N$_0$NP shows a short plateau at 2.4 V followed by a sloping voltage curve until 2.0 V and a long intercalation plateau at 1.1 V versus Na$^+$/Na^0 with a total first discharge capacity of 200 mAh g^{-1} (which is equivalent to 3.5 moles of Na-ions per formula unit (*pfu*)) (Figure 1a). On the subsequent charge, it provides a capacity of only 140 mAh g^{-1}, accounting for an initial Coulombic efficiency (CE) of 70%. The lower CE is attributed to the partial entrapment of Na-ions in the host lattice, electrolyte decomposition, and SEI formation.[25] The corresponding dQ/dV profiles display two redox peaks at 2.4 and 1.2 V versus Na$^+$/Na^0, which could be tentatively ascribed to the operation of Nb^{5+}/Nb^{4+} and Nb^{4+}/Nb^{3+} multi-redox couples (Figure 1c). During the successive ten cycles, the shape of N$_0$NP voltage–capacity profiles is almost maintained with a capacity retention of 97%.

Further, to enhance the Na-ion storage capacity of the same anode, we extended the lower cutoff voltage to 1.0 V versus Na$^+$/Na^0. While it displays similar voltage profiles compared to the 1.1 V versus Na$^+$/Na$^\circ$ cutoff voltage case, the first cycle reversible capacity is slightly enhanced to 154 mAh g^{-1} (which is equivalent to 2.7 moles of Na-ions *pfu*) (Figure 1b). However, we notice drastic changes in the shape of voltage profiles (i.e., loss of voltage plateaus) along with the rapid capacity fade (i.e., 84% retention after ten cycles at C/2 rate) during the subsequent cycles, which could be better viewed from the dQ/dV plots (Figure 1d). Upon cycling at 1C rate (Figure 1e), the N$_0$NP anode undergoes rapid capacity decay in the window of 3.0–1.0 V compared to the 3.0–1.1 V window (39% vs 61% capacity retention after 200 cycles).

To better understand the reason for the contrasting cycling performances of N$_0$NP across the two voltage windows, we performed ex situ XRD and XAS measurements on the cycled anodes (i.e., after ten cycles). The peak intensities of the XRD pattern of N$_0$NP anode cycled in the 3.0–1.0 V window significantly reduced compared to its counterpart in the 3.0–1.1 V window (Figure 1f), implying severe structural degradation. Moreover, the Le-Bail fitting of the XRD patterns reveals elongation of the *c*-axis for the cycled anodes compared to the pristine electrode (Table S1, Supporting Information), due to the removal of Na-ions from Na(1) site, which in turn increases the electrostatic repulsion between oxygen ions of NbO$_6$ octahedra. Fourier-transformed extended X-ray absorption fine structure (FT-EXAFS) spectra collected on the anode cycled in the 3.0–1.0 V window corroborate the XRD observation (Figure 1g), which show the reduction of peak intensities of the first (Nb-O) and second (Nb-Na/P) shells at ≈1.6 and 2.3–3.0 Å, respectively, compared to the pristine electrode (Figure 1g). Further, fitting of the FT-EXAFS spectra reveals significant (i.e., one order of magnitude higher) NbO$_6$ octahedral
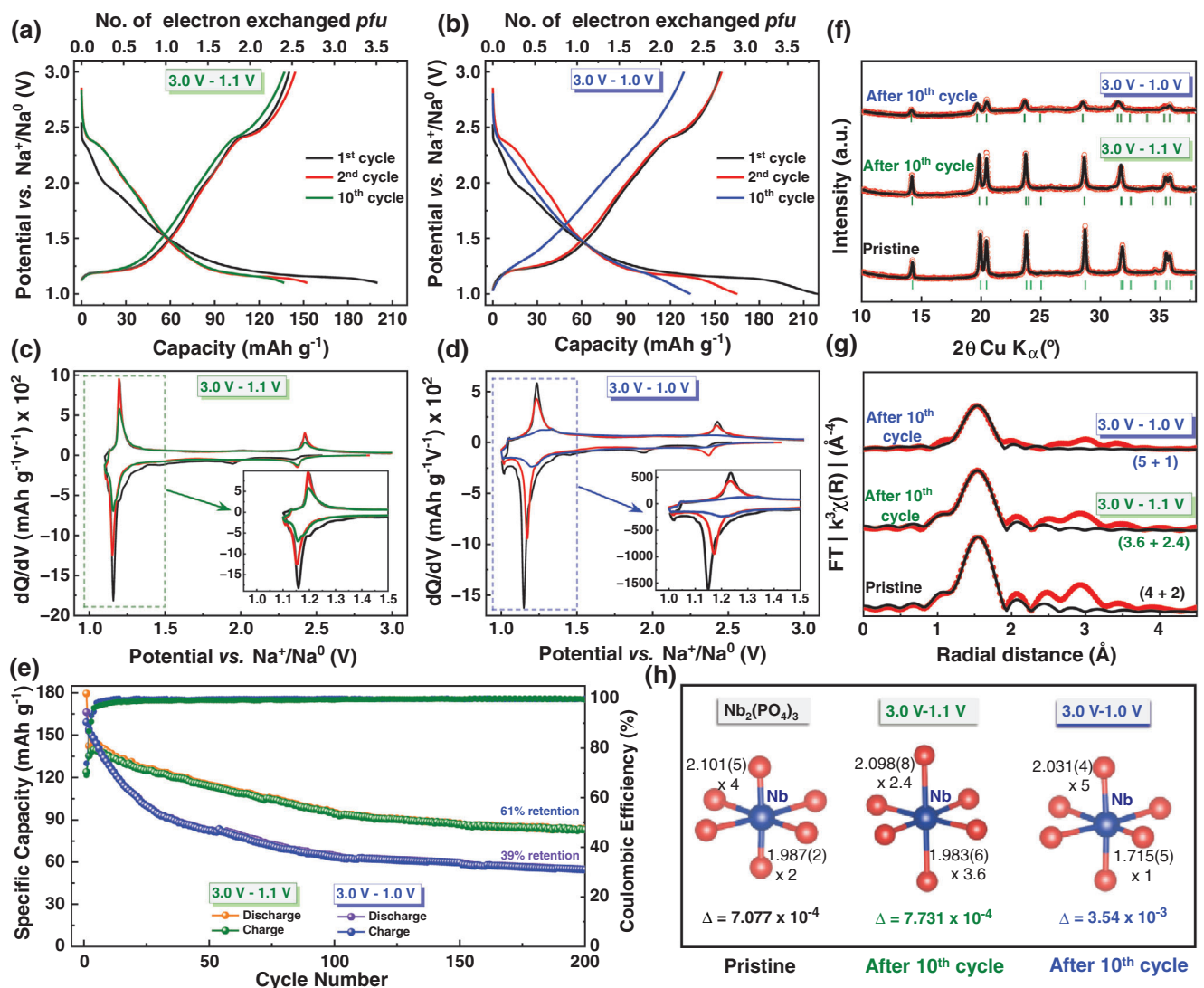
**ADVANCED
SCIENCE NEWS**

www.advancedsciencenews.com

**ADVANCED
ENERGY
MATERIALS**

www.advenergymat.de

Figure 1. a, b) Voltage–capacity, c, d) dQ/dV profiles, and e) capacity retention of N_0NP anode in different voltage windows. f) XRD patterns and g) FT-EXAFS collected at the Nb K-edge, and h) local environment of NbO_6 in the pristine and cycled N_0NbP anodes at different voltage windows.

distortion (Δ) in the 3.0–1.0 V window cycled anode compared to the pristine state (Figure 1h; Figure S2 and Table S2, Supporting Information). On the contrary, the same anode maintains its structural integrity (during the first ten cycles) in the 3.0–1.1 V window, as inferred from its XRD and XAS data.

The poor capacity retention of N_0NbP anode can be ascribed to its severe structural degradation upon electrochemical cycling (especially with the wider voltage window). The N_0NbP host undergoes multiple two-phase electrochemical (de)sodiation reactions with concomitant redox activity of $Nb^{5+}/Nb^{4+}/Nb^{3+}$ centers.[25] During cycling, the sodium ions progressively (de)insert into Na(1) and Na(2) sites of the N_0NbP anode and the possible lack of sufficient Na ions at the Na(1) site may trigger severe NbO_6 octahedral distortion and structural degradation, as deduced from our XAS and XRD studies. Similar degradation of cycle life has been observed when sodium ions have been removed from the Na(1) site in NVP-based cathodes (e.g., $Na_4VMn(PO_4)_3$, $Na_3VCr(PO_4)_3$, $Na_4FeV(PO_4)_3$, etc.).[32–35]

Hence, we attempt to improve the cycle life of N_0NbP anode by introducing Na-ions at the Na(1) site, through partial replacement of Nb^{5+} with V^{3+}. Na ions are introduced into the Na(1) site, which is located between $(Nb/V)O_6$ octahedra, to act as a pillar to maintain structural integrity.

We synthesized two NASICON compositions, namely $Na_{1.25}V_{0.25}Nb_{1.75}(PO_4)_3$ and $Na_{1.5}V_{0.5}Nb_{1.5}(PO_4)_3$ using the solid-state route (for details, see Experimental Section). The XRD pattern of the Na-filled NASICON compounds can be well indexed with the NASICON $R\bar{3}c$ structure (**Figure 2a**; Figure S3, Supporting Information). We performed Rietveld refinements on the XRD patterns of $N_{1.25}VNbP$ and $N_{1.5}VNbP$ compounds to understand their structural evolution upon cationic substitutions and the corresponding crystallographic parameters are listed in Table S3 (Supporting Information). The crystal structures of $N_{1.25}VNbP$ and $N_{1.5}VNbP$ are built by lantern units, consisting of two $(Nb/V)O_6$ octahedra and three PO_4 units stacked along the c-direction (Figure 2b). Na-ions occupy two distinct

ADVANCED
SCIENCE NEWS

www.advancedsciencenews.com
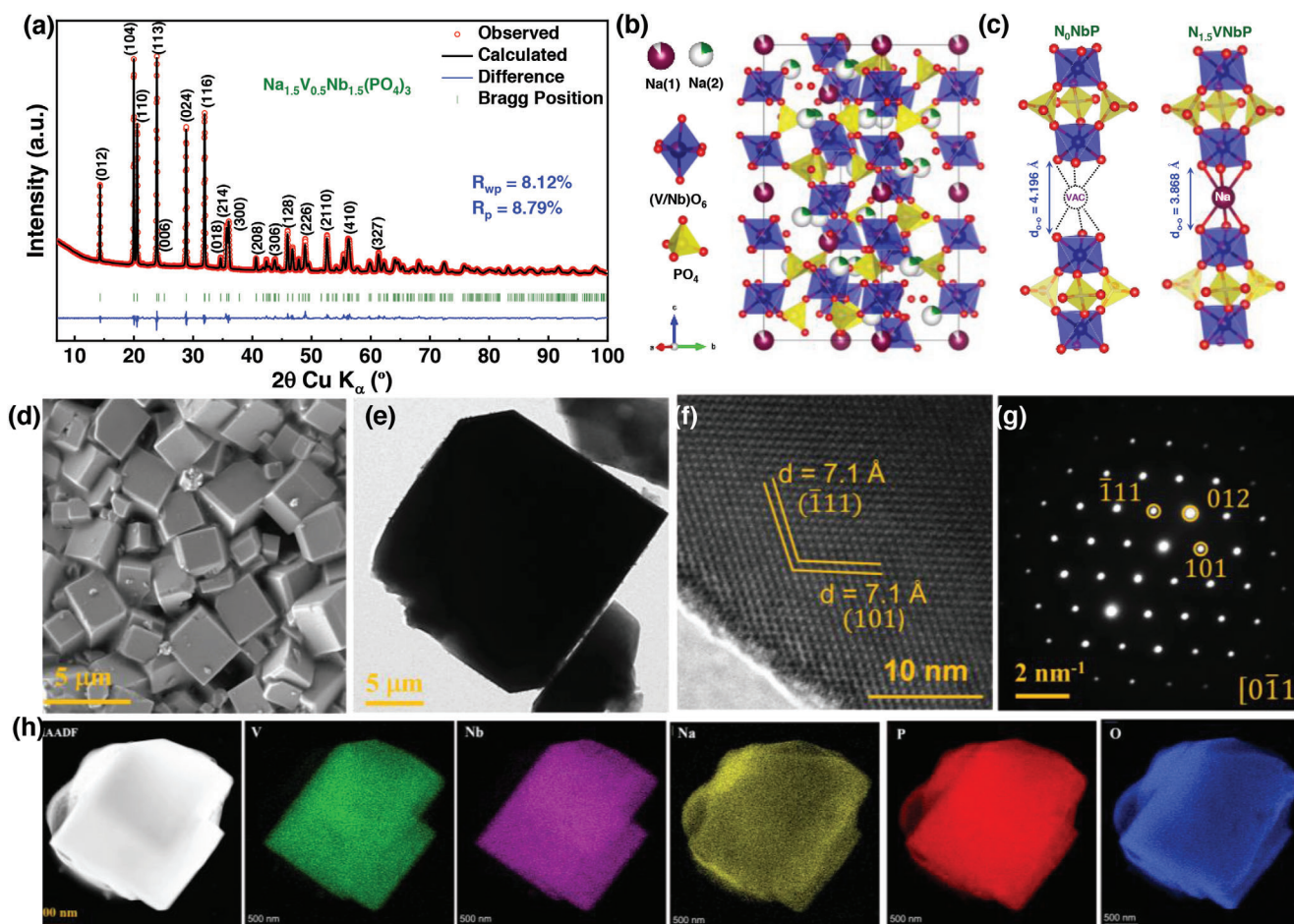
ADVANCED
ENERGY
MATERIALS

www.advenergymat.de

Figure 2. a) Rietveld refined XRD pattern and b) crystal structure of NASICON-$N_{1.5}$VNbP. c) Comparison of O(2)—O(2) bond distances between (V/Nb)O_6 octahedra of N_0NbP and $N_{1.5}$VNbP. d) SEM, e) low magnification TEM, f) HRTEM images and g) SAED pattern of $N_{1.5}$VNbP anode. h) HAADF-STEM image and elemental mapping of $N_{1.5}$VNbP anode.

crystallographic sites in the 3D framework: Na(1) and Na(2). Na(1)/Na(2) occupancies are estimated as 0.829/0.113 and 0.758/0.212 for the $N_{1.25}$VNbP and $N_{1.5}$VNbP compositions, respectively, which are slightly lower than the target values. More significantly, the bond distance of O(2)—O(2) diminishes as the Na-ions fill into Na (1) sites (see Table S4, Supporting Information), indicating the suppression of the electrostatic repulsion between oxygen layers of (V/Nb)O_6 (Figure 2c).

Further, to probe the changes in oxidation states and coordination environments of vanadium and niobium cations, we perform XAS analyses on the $N_{1.25}$VNbP and $N_{1.5}$VNbP anodes. The normalized absorption spectra collected at Nb and V K-edges are displayed in Figure S4 (Supporting Information). The energies calculated from the first derivative of inflection points of the corresponding spectra confirm the mixed oxidation states of niobium (i.e., Nb^{5+} and Nb^{4+}) and V^{3+} in the $N_{1.25}$VNbP and $N_{1.5}$VNbP anodes. We also confirm the presence of mixed valance Nb^{5+}/Nb^{4+} through XPS measurements (Figure S5, Supporting Information). Two doublets of Nb $3d_{5/2}$ and Nb $3d_{3/2}$ are noticed at 208.7/211.7 and 207.8/210. eV, respectively, which corresponds to Nb^{5+} and Nb^{4+}, confirming the mixed oxidation of niobium at the surface of the anode. The V 2p spectra enlist two primary

peaks at 517.0 eV (V-$2p_{3/2}$) and 523.8 eV (V-$2p_{1/2}$) with a satellite peak (Figure S5b, Supporting Information), suggesting the existence of V^{3+} in both $N_{1.5}$VNbP and $N_{1.25}$VNbP samples. We suspect that high-temperature annealing causes Na deficiency in the NASICON host as observed in our XRD analyses, which results in the oxidation of Nb^{4+} to Nb^{5+}. Additionally, FT-EXAFS of NASICON anodes are shown in Figure S6 (Supporting Information) along with their theoretical fits. The peaks ≈1.5 and 2–3.25 Å represent the first (V/Nb)-O and second (V/Nb)-(Na/P) shells, respectively. While the EXAFS fitting reveals minor changes in the average (V/Nb)—O bond distances (≈1.994–1.998 Å) (Tables S5 and S6, Supporting Information), the (V/Nb)O_6 coordination environment changes from [4+2] for $Nb_2(PO_4)_3$ to [3.3+2.7] for the $N_{1.25}$VNbP and [3.5+2.5] for the $N_{1.5}$VNbP due to the occupation of Na-ions at Na(1) site. Overall, the filling of Na(1) site reduces the electrostatic repulsion between oxygen layers of (V/Nb)O_6, which can stabilize the NASICON host lattice during cycling.

Microscopy analyses reveal that the $N_{1.25}$VNbP and $N_{1.5}$VNbP anodes consist of cube-like micron-sized particles (≈0.8–3.4 μm) (Figure 2d; Figure S7, Supporting Information). The high-resolution TEM (HRTEM) image shows the interference fringes corresponding to d-spacing of ≈7.1 Å, which belong to the
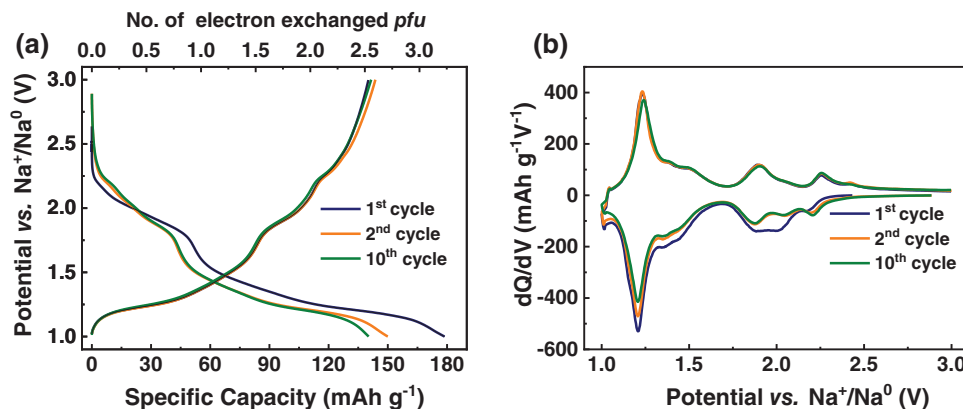
**ADVANCED
SCIENCE NEWS**

www.advancedsciencenews.com

**ADVANCED
ENERGY
MATERIALS**

www.advenergymat.de

Figure 3. a) Voltage–capacity and b) dQ/dV profiles of $N_{1.5}$VNbP anode.

($\bar{1}11$) and (101) planes of $N_{1.5}$VNbP anode (Figure 2e–f), which indicates the single-crystalline nature of particles. The same observation is also confirmed by the sharp diffraction spots observed in selected area electron diffraction (SAED) (Figure 2g). The homogenous distribution of elements (Na, Nb, V, P, and O) in the cube particles is confirmed through high-angle annular dark-field (HAADF)-scanning transmission electron microscopy (STEM) elemental mapping (Figure 2h). Further, the chemical compositions of the $N_{1.25}$VNbP and $N_{1.5}$VNbP anodes are estimated as $Na_{1.148}V_{0.234}Nb_{1.764}(PO_4)_3$ and $Na_{1.372}V_{0.443}Nb_{1.564}(PO_4)_3$, respectively, through inductively coupled plasma optical emission spectrometer (ICP-OES) measurements.

The $N_{1.25}$VNbP and $N_{1.5}$VNbP anodes exhibit multi-step voltage–capacity profiles with reversible capacities of 135–140 mAh g^{-1} in the window of 3.0–1.0 V versus Na$^+$/Na^0 at C/5 rate, which are closer to their theoretical capacities ($\approx$140–150 mAh g^{-1}, based on V^{3+}/V^{2+} and Nb^{5+}/Nb^{4+}/Nb^{3+} redox) (**Figure 3a**; Figure S8a, Supporting Information). Accordingly, their corresponding dQ/dV profiles contain multiple redox features. The redox peaks located at lower voltages, $\approx$1.2 and $\approx$1.6 V, are ascribed to Nb^{4+}/Nb^{3+} and V^{3+}/V^{2+} redox couples (Figure 3b; Figure S8b, Supporting Information).[25,36] Additionally, we also notice smaller voltage features in the range of 2.3–1.75 V, which could be presumably attributed to the redox activity of Nb^{5+}/Nb^{4+} couple. The Na (de)intercalation mechanism of $N_{1.25}$VNbP and $N_{1.5}$VNbP anodes was further studied by cyclic voltammetry experiments (Figure S9, Supporting Information). Their corresponding voltammograms display similar redox features compared to the dQ/dV plots, confirming the reversible (de)intercalation through the activity of Nb^{5+}/Nb^{4+}/Nb^{3+} and V^{3+}/V^{2+} multi-redox centers. More significantly, the voltage–capacity and dQ/dV profiles of the $N_{1.25}$VNbP and $N_{1.5}$VNbP anodes neatly superimpose on each other during the first ten cycles, unlike the $Nb_2(PO_4)_3$, implying an enhanced structural stability of V-substituted NASICON framework. The hypothesis of better structural integrity with V-substitution is further verified with XRD and XAS data, which show no noticeable changes between the cycled and pristine electrodes (Figures S10 and S11, Table S6, Supporting Information). Further, we also carried out TEM studies to understand the structural changes in the cycled $N_{1.5}$VNbP anode (Figure S12, Supporting Information). The HRTEM im-

age shows the lattice fringes with d-spacings of $\approx$4.3 and 7.3 Å, corresponding to (110) and (006) planes, respectively. Likewise, the SAED pattern displays the presence of (110), (113), and (003) planes along [$\bar{1}$10] zone axis. Altogether, the TEM studies confirm the retention of crystallinity after the electrochemical cycling, corroborating our XRD and XAS findings.

To understand the Na-ion intercalation mechanism in the $N_{1.25}$VNbP and $N_{1.5}$VNbP anodes, we performed in situ XRD measurements at C/10 rate (**Figure 4a**). The most intense reflections of the $N_{1.5}$VNbP anode such as (104), (110), (113), (024), (116), (214), and (300) progressively shift toward to lower and higher 2θ values, during discharge and charge processes, respectively. Moreover, the unit cell volume of the $N_{1.5}$VNbP anode smoothly varies during cycling, indicating the formation of complete solid-solution between $Na_{1.5}V_{0.5}Nb_{1.5}(PO_4)_3$ and $Na_{4.0}V_{0.5}Nb_{1.5}(PO_4)_3$ endmembers with an overall volume change of 9.3% (Figure 4b). A comparison between simulated and experimental XRD patterns reveals that the Na(2) sites are predominantly filled (from 0.22 to 1.0) during the discharge process, while the occupancy at Na(1) site is maintained between 0.88 and 1.0 (Figure S13, Supporting Information).

The formation of solid-solution is further confirmed by the PITT measurement, which shows characteristic Cottrelian current responses during the cycling process (Figure 4c).[37,38] Similar solid-solution formation is also noticed for the $N_{1.25}$VNbP anode during the Na-ion (de)intercalation, but with a narrower two-phase region (2.6 < x < 3.0) (Figure S14, Supporting Information). The changes in the redox states of V and Nb in the $N_{1.5}$VNbP anode during the cycling were monitored by XAS. The corresponding normalized X-ray absorption near edge structure (XANES) spectra are provided in Figure 4d,e, respectively. As the discharge proceeds, the Nb and V K-edges shift toward lower energies, indicating the reduction of Nb^{5+}/Nb^{4+} to Nb^{3+} and V^{3+} to V^{2+}. Subsequently, the Nb and V K-edges return to their original positions at the end of the charging process, implying that the Na (de)intercalation process is completely reversible. The changes in the oxidation states of Nb redox in the $N_{1.5}$VNbP anode is also monitored through ex situ XPS (Figure S15, Supporting Information). The coexistence of Nb^{5+} (208.9 eV) and Nb^{4+} (207.7 eV) in the pristine electrode is revealed from the Nb3d$_{5/2}$ peak. Upon discharging to 1.7 V, the Nb3d$_{5/2}$ peak shifts to lower energy indicating reduction of Nb^{5+} to Nb^{4+}. On the complete discharge
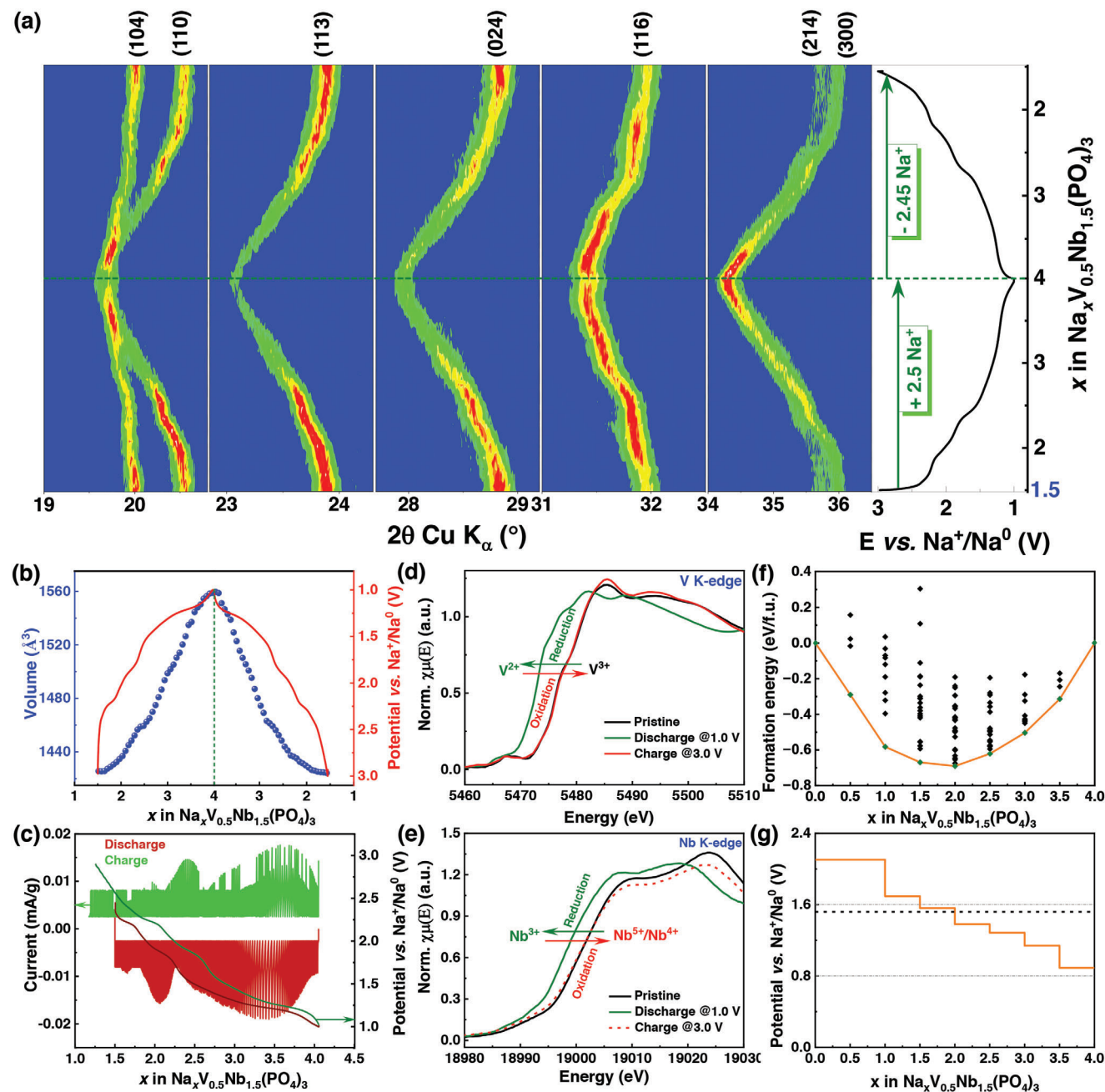
Figure 4. a) Intensity contour map of in situ XRD patterns and b) evolution of unit cell volume of $N_{1.5}VNbP$ anode during the second cycle. c) Voltage and specific current response of the sodium-ion (de)intercalation into $N_{1.5}VNbP$ anode utilizing PITT protocol. XANES of $N_{1.5}VNbP$ anode collected at d) V and e) Nb K-edges at different state-of-charges. f) DFT-calculated 0 K convex hull for $Na_xV_{0.5}Nb_{1.5}(PO_4)_3$ with formation energy (in eV/f.u.) plotted as a function of Na-ion concentration, x in $Na_xV_{0.5}Nb_{1.5}(PO_4)_3$. Orange line represents the convex hull. Green (black) diamonds represent the stable ground states (metastable) states lying on (above) the hull for each x. g) The calculated Na (de)intercalation voltage profile as a function of Na-ion concentration (x in $Na_xV_{0.5}Nb_{1.5}(PO_4)_3$). The black dashed line represents the predicted average voltage (V_{avg} = 1.52 V vs Na) across x = 0 to x = 4.

to 1.0 V, the reduction to Nb^{3+} is noticed, and the subsequent charge to 3.0 V, the $Nb3d_{5/2}$ peak returns to its initial position, suggesting the reversibility of Na (de)intercalation.

We performed DFT calculations (for details, see computational section) to contextualize our experimental findings of Na-ion (de)intercalation in the $N_{1.5}VNbP$ anode. The DFT-calculated 0 K convex hull (Figure 4f) is constructed based

on formation energies of possible configurations across the entire $Na_xV_{0.5}Nb_{1.5}(PO_4)_3$ compositional space ($0 \leq x \leq 4$; in Δx = 0.5 steps). Notably, the convex hull highlights the set of stable ground state configurations, indicated by green diamonds in Figure 4f, with $Na_0V_{0.5}Nb_{1.5}(PO_4)_3$ (fully desodiated) and $Na_4V_{0.5}Nb(PO_4)_3$ (fully sodiated) as terminal compositions. For every unique x, the corresponding $Na_xV_{0.5}Nb_{1.5}(PO_4)_3$

composition exhibits a stable configuration that lies on the hull, except for x = 0.5, which is in alignment with the experimentally observed reversible, solid-solution behavior of Na (de)intercalation, i.e., $Na_{1.5}V_{0.5}Nb_{1.5}(PO_4)_3 \leftrightarrow Na_{4.0}V_{0.5}Nb_{1.5}(PO_4)_3$.

Notably, all ground states from x = 1 have fully occupied Na(1) sites, with Na occupancy of the Na(2) sites increasing monotonically with x from x = 1 to x = 4. Based on the convex hull, we estimate the Na (de)intercalation voltage profile (Figure 4g) in the $Na_xV_{0.5}Nb_{1.5}(PO_4)_3$ anode. We obtain an average Na intercalation voltage, across the x = 0 to x = 4 range to be 1.52 V versus Na. The voltage plateau between x = 0 and x = 1 (at 2.10 V vs Na), indicates the instability of the x = 0.5 composition. Importantly, beyond x = 1.5, the voltage profile is made of several "small" voltage steps (< 0.2 V), as the Na (de)intercalation traverses through the ground state configurations in Δx = 0.5 steps. Notably, the small voltage steps between x = 1.5 and x = 4 may diminish at higher temperatures to a "smooth" voltage profile due to entropic contributions,[39] giving rise to a solid-solution-like voltage profile, as observed in our XRD and PITT experiments (Figure 4a–c).

Using the on-site calculated magnetic moments on the Nb and V transition metal centers, we also tracked the redox activity of the Nb and V ions with Na addition into the $Na_xV_{0.5}Nb_{1.5}(PO_4)_3$ structure. At x = 0, we indeed observe Nb and V to be in their +5 and +3 oxidation states, respectively, based on calculated on-site magnetic moments of ≈0.01–0.02 μ_B on Nb and ≈1.79 μ_B on V. For Na additions up to x = 1.5, the Nb undergoes reduction while V remains inactive, with all Nb in the unit cell considered exhibiting a +4 oxidation state at x = 1.5, indicated by an absolute magnetic moment of ≈0.85–0.88 μ_B. Subsequently, V undergoes reduction for Na addition from x = 1.5 to x = 2, with V displaying a magnetic moment of ≈2.58 μ_B at x = 2. Thus, V shows redox-activity only from the x = 1.5 to 2 Na composition range and remains inactive for other Na contents. Further, Na additions from x = 2 up to x = 3.5 result in different Nb metal centers being sequentially reduced, with all Nb attaining a +3 oxidation state at x = 3.5 (magnetic moment ≈1.68–1.71 μ_B). The final addition of Na from x = 3.5 to x = 4 gives rise to Nb reduction from +3 to +2. However, due to electronic delocalization among Nb metal centers at x = 4, the resultant magnetic moments are ambiguous on the Nb sites (i.e., either ≈1.71 or ≈2.01 μ_B). As a result, we are unable to distinctly assign the specific Nb sites that undergo reduction from +3 to +2 as Na intercalates from x = 3.5 to 4. The observed trends of V- and Nb-redox activities from theory is in agreement with the electrochemical measurements.

Next, we turn our attention towards optimizing the electrochemical performance of $N_{1.25}$VNbP and $N_{1.5}$VNbP anodes in different electrolyte solutions ($NaBF_4$/diglyme, $NaPF_6$/diglyme and $NaClO_4$/carbonate). The voltage–capacity profiles of both NASICON anodes collected at C/5 rate are displayed in Figure S16 (Supporting Information). The $N_{1.5}$VNbP anode exhibits higher initial Coulombic efficiencies (ICEs) in diglyme-based electrolytes compared to the carbonate solution (77%, 75.3%, and 60.8% in $NaBF_4$/diglyme, $NaPF_6$/diglyme, and $NaClO_4$/carbonate, respectively), suggesting lesser entrapment of sodium ions during the SEI formation. Similar trends in ICEs are noticed for the $N_{1.25}$VNbP anode as well. Moreover, both anodes exhibit lowest charge transfer resistance (Rct) values in diglyme-based electrolytes (Figures S17 and S18, Table S7, Supporting Information), implying facile Na-ion intercalation compared to the carbonate system.[40,41]

Upon continuous cycling, the $N_{1.5}$VNbP anode exhibits superior capacity retentions across different electrolytes compared to the $N_{1.25}$VNbP (**Figure 5a**; Figure S19, Supporting Information), signifying our strategy to introduce extra sodium-ions into NASICON host for maintaining the structural stability. The $N_{1.5}$VNbP anode delivers discharge capacities of 120 and 130 mAh g^{-1} at 1C rate and show capacity retentions of 82% and 78% at the end of 200 cycles in $NaBF_4$/diglyme and $NaPF_6$/diglyme solutions, respectively (Figure 5a). On the other hand, the $N_{1.25}$VNbP anode maintains 73% and 67% of its initial capacity after 200 cycles at 1C rate in $NaBF_4$/diglyme and $NaPF_6$/diglyme, respectively (Figure S19, Supporting Information). Even with higher C-rate (i.e., 5C), the $N_{1.5}$VNbP anode exhibits extraordinary cycling stabilities (89% and 81%, after 500 cycles $NaBF_4$/diglyme and $NaPF_6$/diglyme, respectively) compared to the $N_{1.25}$VNbP anode (Figure 5a; Figure S19, Supporting Information). Another interesting observation from the electrolyte optimizing studies is that both anodes display inferior capacity retentions in $NaClO_4$/carbonate electrolyte (74% and 45% for the $N_{1.5}$VNbP and $N_{1.25}$VNbP anodes after 200 cycles at 1C rate), implying the nature of the formed SEI may influence the stability of NASICON anodes during cycling.

To understand the contrasting cycling stabilities of the $N_{1.5}$VNbP in diglyme- and carbonate-based electrolytes, we performed XRD, SEM and XPS studies on the cycled anodes. The anode maintains excellent structural integrity (after 200 cycles) upon cycling in diglyme-based electrolyte, as deduced from its XRD and SEM results (Figures S20 and S21, Supporting Information). Similarly, the crystalline structure and morphology of the anode are also retained during the cycling in carbonate-based electrolyte (Figures S20 and S21, Supporting Information). Since the XRD and SEM studies cannot explain the reason for the cycling (in)stabilities, we suspect the formation of stable solid electrolyte interphase (SEI) on the $N_{1.5}$VNbP anode could be the key for its capacity retention.[42,43] Therefore, to understand the compositions of SEI formed in both electrolytes, we performed XPS studies on the cycled anodes. The deconvoluted C 1s, O 1s, and F 1s spectra of the anodes collected after tenth cycles are provided in **Figure 6d–f**. The C 1s spectrum of anode cycled in diglyme-based electrolyte displays prominent peaks at 284.6 (—C—C—) and 286 eV (—C—O—), which can be ascribed to the formation of sodium alkoxides (RCH$_2$ONa) from the decomposition of diglyme. The other two peaks located at 288 (—C—O—C—) and 289.3 eV (—CO$_3$) are due to the formation of polyethers and Na$_2$CO$_3$, respectively.[43–46] The presence of RCH$_2$ONa (534 eV) and Na$_2$CO$_3$ (531.6 eV) is also inferred from the O 1s spectra. The F 1s spectrum shows two distinct peaks at 687.4 and 684.6 eV, corresponding to B—F and Na—F species, respectively. Overall, the SEI arising from the decomposition of $NaBF_4$/diglyme consists of organic (RCH$_2$ONa, polyether) and inorganic species (NaF, Na$_2$CO$_3$, NaBF$_4$).[41,43,47–50]

The XPS spectra of the anode cycled in carbonate-based electrolyte also display similar components, except a distinct peak corresponding to sodium alkyl carbonate (ROCO$_2$Na, 286.6 eV) in the C 1s spectra. The F1s spectrum shows the presence of NaF due to the decomposition of the FEC additive. Previous reports attributed the dissolution of Na$_2$CO$_3$ in carbonate

ADVANCED
SCIENCE NEWS

www.advancedsciencenews.com

ADVANCED
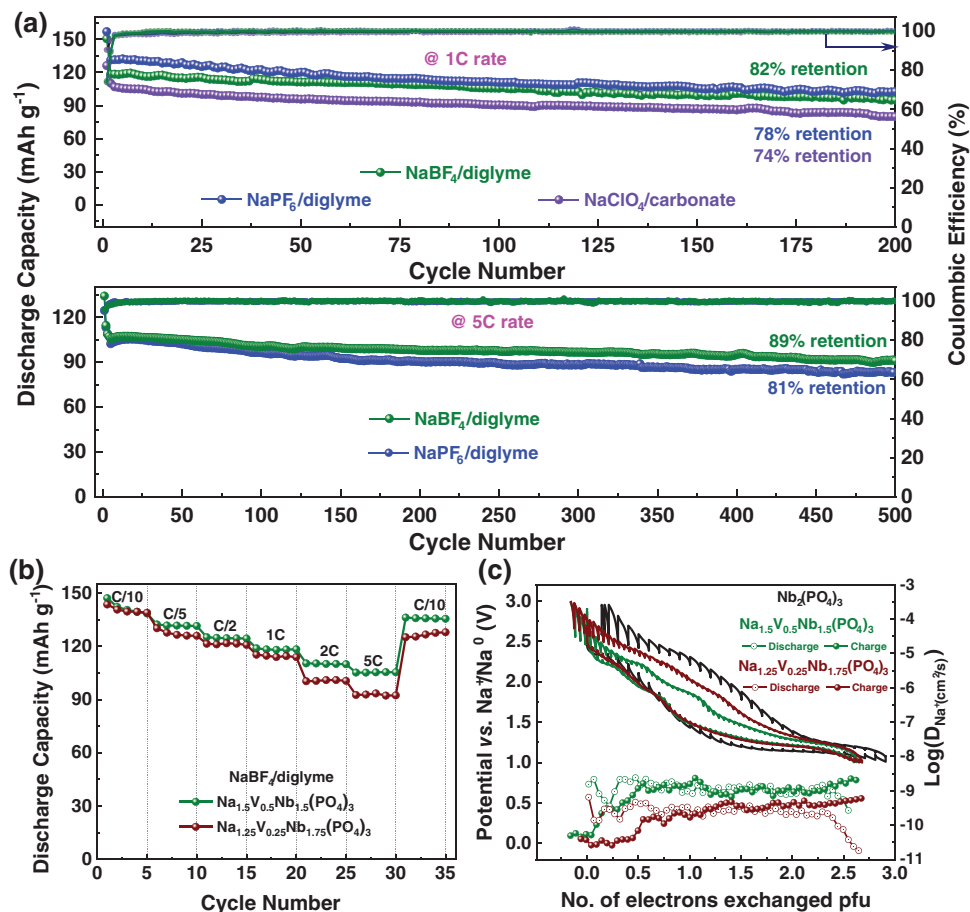**ENERGY**
MATERIALS

www.advenergymat.de

Figure 5. a) Long-term cycling stabilities of the $N_{1.5}$VNbP anode at 1C and 5C rates. b) Rate performances from 0.1C to 5C of the $N_{1.5}$VNbP (1C = 138 mA g^{-1}) and $Na_{1.25}$VNbP (1C = 150 mA g^{-1}) anodes. c) Comparison of galvanostatic intermittent titration technique (GITT) profiles of N_0NbP, $N_{1.25}$VNbP and $N_{1.5}$VNbP with Na$^+$ diffusion coefficient (D_{Na^+}) calculated from GITT profiles as a function of voltage and number of electrons exchanged for both the charge and discharge processes.
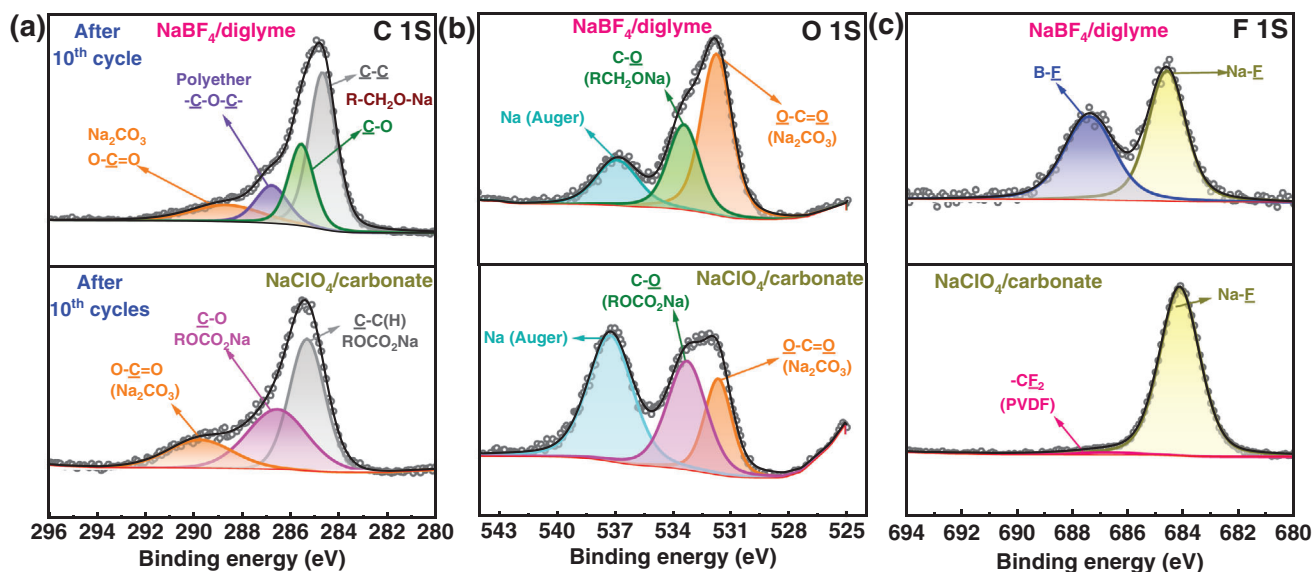
Figure 6. X-ray photoelectron spectroscopy (XPS) spectra a) C 1s, b) O 1s, and c) F 1s collected on the $N_{1.5}$VNbP anodes cycled in different electrolytes.

electrolyte to the poor SEI stability and rapid capacity loss of Na-ion anodes.[41,51] In the case of diglyme electrolyte, sodium alkoxides (RCH_2ONa) ensure fast Na^+ transport and is essential for the interfacial and structural stability of the Na anodes.[41,43] The impact of SEI (in)stability on the electrochemical performance of NASICON anode is further elucidated with the electrochemical impedance spectroscopy (EIS) measurements (see Figure S22 for details, Supporting Information). Upon continuous cycling in $NaBF_4$/diglyme electrolyte, the charge transfer resistance (R_{ct}) of the $N_{1.5}VNbP$ anode initially decreases (from 44.7 to 16.6 Ω within the first 25 cycles) and remains stable ≈20 Ω up to 150 cycles (Table S7, Supporting Information). However, the R_{ct} values continuously increase from 30.28 (after 25th cycle) to 64.93 Ω (after 150th cycle) in carbonate electrolyte due to unstable SEI. Altogether, pairing the $N_{1.5}VNbP$ anode with diglyme-electrolyte results in impressive cycling stability, thanks to the lower R_{ct} and the stable SEI.

We also tested the rate capabilities of $N_{1.25}VNbP$ and $N_{1.5}VNbP$ anodes in $NaBF_4$/diglyme electrolyte. Their corresponding voltage versus capacity profiles and rate performance plots at different C-rates are displayed in Figure S23 (Supporting Information). The $N_{1.5}VNbP$ anode displays superior rate performances across different C-rates compared to the $N_{1.25}VNbP$. The $N_{1.5}VNbP$ anode delivers discharge capacities of 140, 132, 125, 120, 110, and 105 mAh g^{-1} at C/10, C/5, C/2, 1C, 2C, and 5C rates, respectively, whereas the $N_{1.25}VNbP$ provides 138, 127, 121, 114, 98, and 89 mAh g^{-1} under similar experimental conditions (Figure 5b). To better understand the outstanding rate performance of the $N_{1.5}VNbP$ anode, we perform GITT measurements (Figure 5c). The GITT profile of $N_{1.5}VNbP$ shows significantly lower polarization between charge and discharge process compared to those of $N_{1.25}VNbP$ and N_0NbP anodes, implying improved Na (de)intercalation kinetics (or better Na diffusivity) due to the introduction of additional Na-ions in the host.

The diffusion coefficient (D_{Na+}) of $N_{1.5}VNbP$ anode calculated from the GITT experiment (Figure S24, Supporting Information) is found to be ≈10^{-9} cm^2 s^{-1}, at least an order of magnitude higher than that of $Na_{1.25}V_{0.25}Nb_{1.75}(PO_4)_3$ (≈10^{-10}–10^{-11} cm^2 s^{-1}). Earlier reports showed that the Na-ion ionic conductivities in NASICON frameworks, which is directly related to diffusivity of Na, non-monotonically increase from a Na content of ≈1 mole *pfu* to ≈3.4 moles *pfu* and subsequently decrease as the Na content reaches 4 moles *pfu*.[52–54] The non-monotonic behavior of Na-conductivities is due to the decrease of both migration barriers and concentration of diffusion carriers (i.e., Na-vacancies) as the Na concentration increases within the NASICON structure. Given the similar ionic nature of different NASICON chemistries, we can expect similar trends in Na diffusivities to hold in our N_xVNbP material as well, possibly explaining our observation of higher Na-diffusivity in $N_{1.5}VNbP$ compared to $N_{1.25}VNbP$.

Inspired by the extraordinary cycling stability and rate performances of $N_{1.5}VNbP$, we fabricated a full Na-ion cell using the NVP and $N_{1.5}VNbP$ as the cathode and anode, respectively (see experimental section for details). The NVP cathode typically delivers reversible capacities of ≈108 mAh g^{-1} at 3.4 V versus Na^+/Na^0.[24] Coupling NVP cathode and $N_{1.5}VNbP$ anode produces an average cell voltage of ≈1.9 V (**Figure 7a**), which is

the highest value among the NASCION-based Na-ion cells (i.e., both electrodes with NASICON structures).[19,28–31] Figure 7b displays the charge/discharge profiles of the NVP‖$N_{1.5}VNbP$ Na-ion cell from the first ten cycles at C/10 rate. The cell reversibly delivers stable capacities of ≈104 mAh g^{-1} at an average voltage of ≈1.9 V at C/10 rate, rendering an impressive energy density of 98 Wh kg^{-1} (based on the mass of cathode and anode) compared to the other NASICON-based SIBs (Table S8, Supporting Information). The corresponding dQ/dV profile of the Na-ion full cell entails four pairs of redox features at 2.15, 1.9, 1.5, and 1.15 V due to the operation of multi-redox centers at the anode (Figure S25, Supporting Information). Further, the full cell delivers discharge capacities of 105, 102, 94, 89, 80, and 70 mAh g^{-1} at C/10, C/5, C/2, 1C, 2C and 5C, respectively (Figure 7c,d) and recovers back to 100 mAh g^{-1} of capacity upon reversing the C-rate to C/10. The full Na-ion delivers 91 mAh g^{-1} during the initial cycles and retains 86% of the capacity after 200 cycles at 1C rate (Figure 7e). Upon increasing the C-rate to 5C, the Na-ion cell demonstrates extraordinary cycling stability with 80% of capacity retention after 1000 charge/discharge cycles. It is worth noting that the cycling stability and rate performances of NVP‖$N_{1.5}VNbP$ cell is comparable (or even superior) to other NASICON-based Na-ion cells (Table S8, Supporting Information).[19,28–31]

3. Conclusion

In summary, we have used a structural modulation approach, combined with optimizing electrolytes, to improve the electrochemical performance of the multi-electron NASICON-N_0NbP anode via introduction of extra sodium ions at the Na(1) site and a concomitant substitution of Nb^{5+} with V^{3+}. The Na-filled NASICON-$N_{1.5}VNbP$ anode renders reversible capacities of ≈140 mAh g^{-1} at C/10 rate with enhanced structural stability, as determined from XRD, XAS and electrochemical experiments. Upon continuous cycling, the NASICON-$N_{1.5}VNbP$ anode sustains 89% of its initial capacity over 500 cycles at 5C rate, contrasting to the rapid capacity decay of "empty" NASICON-N_0NbP. The extra sodium-ions in the Na-filled NASICON-$N_{1.5}VNbP$ also decrease the voltage polarization between charge and discharge processes, improve sodium diffusion and enable higher rate capabilities. Moreover, the NASICON-$N_{1.5}VNbP$ anode undergoes complete solid-solution formation during Na (de)intercalation, contrasting to the multi-phase behavior of "empty" NASICON-N_0NbP. Our experimental observation of the solid-solution-like Na-intercalation behavior and redox-activity of Nb and V ions is in agreement with DFT calculations. Additionally, we find the diglyme-based electrolytes to generate stable SEI that allows for better cycle life and capacity retention compared to carbonate-based electrolytes. Most importantly, the NASICON-based sodium-ion full cell—NVP‖ $N_{1.5}VNbP$ provides a higher cell voltage of ≈1.9 V, an appealing energy density of 98 Wh kg^{-1} for practical application, and a reasonable cycle life (≈80% capacity retention over 1000 cycles at 5C). Overall, our study demonstrates the utility of chemical and structural modulation to tune and optimize the electrochemical performances of NASICON anodes.
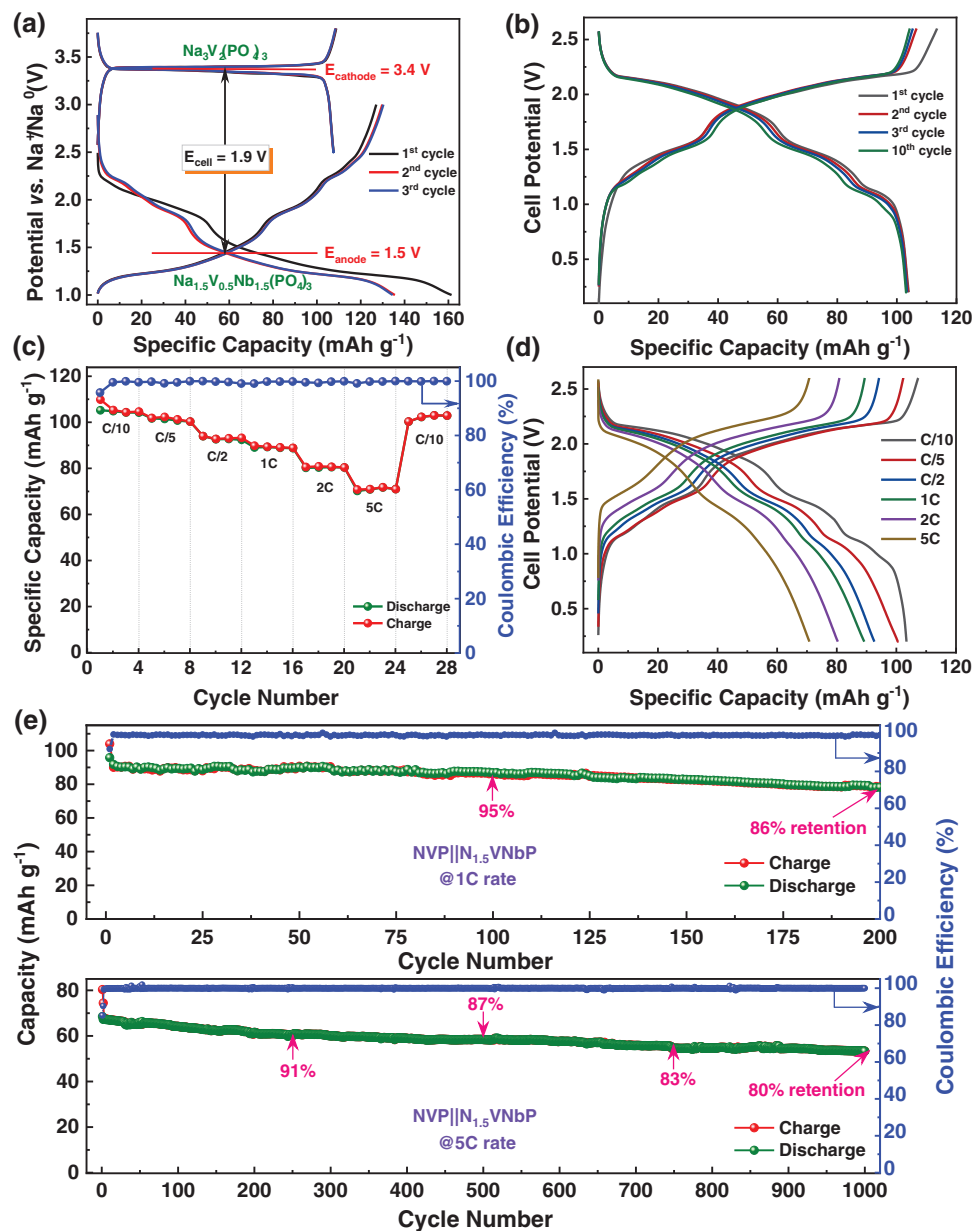
**ADVANCED
SCIENCE NEWS**

www.advancedsciencenews.com

**ADVANCED
ENERGY
MATERIALS**

www.advenergymat.de

Figure 7. Voltage–capacity profiles of a) NVP cathode and $Na_{1.5}$VNbP anode, and b) NVP||$Na_{1.5}$VNbP full Na-ion at C/10 rate. c) Rate performances, e) voltage–capacity profiles at different C-rates (1C = 117 mA g^{-1}), and e) long-term cycling stabilities of NVP||$Na_{1.5}$VNbP full Na-ion cell.

4. Experimental Section

Synthesis: $Nb_2(PO_4)_3$ was synthesized according to the previous report.[25] $N_{1.25}$VNbP ($Na_{1.25}V_{0.25}Nb_{1.75}(PO_4)_3$) and $N_{1.5}$VNbP ($Na_{1.5}V_{0.5}Nb_{1.5}(PO_4)_3$) samples were synthesized through solid-state route. A stoichiometric amount of $(NaPO_3)_6$ (Alfa Aesar, 99%), V_2O_3 (Sigma–Aldrich, 98%), NbO_2 (Alfa Aesar, >99%), and P_2O_5 (Alfa Aesar, 99.0%) were mixed using high-energy ball milling (SPEX 8000M) for 20 min. The ball-milled product was taken in different quartz ampoules. These ampoules were sealed under a high vacuum (10^{-6} mbar) and placed in a muffle furnace. The quartz ampoules were heated at 1000 °C at a rate of 0.5 °C min^{-1} for 24 h and then slowly cooled back to room temperature. The product was taken out by cutting the ampule and ground well using mortar and pestle to get the fine powder as a final product.

Material Characterization: XRD patterns of NASICON anodes were measured using a Rigaku Smart Lab diffractometer (Cu K$_\alpha$; λ = 1.5406 Å) with an accelerating voltage of 40 kV and a current of 30 mA at room temperature. Rietveld refinements were performed on the collected XRD patterns using the FullProf program[55,56] to obtain structural solutions. The field emission scanning electron microscopy (FE-SEM) images were taken using a Zeiss (Gemini SEM 500) microscope. Transmission electron microscopy (TEM; Thermofisher Talos F200 S) operated at 200 keV and equipped with high-angle annular dark field (HAADF) detector and energy dispersive X-ray spectrometer (EDS) was used to analyze morphology and distribution of elements. X-ray photoelectron spectroscopy (XPS) measurements were performed using a Thermofisher K-Alpha instrument with microfocused and monochromated Al Kα radiation with an energy of 1486.6 eV. The binding energy scale was calibrated from the C1s peak

**ADVANCED
SCIENCE NEWS**

www.advancedsciencenews.com

**ADVANCED
ENERGY
MATERIALS**

www.advenergymat.de

at 284.8 eV. The core peaks were fitted using the Avantage software with a nonlinear Shirley-type background. The elemental compositions of the NASICON anodes were determined by an inductively coupled plasma optical emission spectrometer (ICP-OES, PerkinElmer Optima 7000 DV instrument).

Electrochemical Measurements: To prepare the NASICON anodes, the active material and Super C45 (Timcal) were ball milled together in a weight ratio of 75:25 for 15 mins. Polyvinylidene fluoride (PVDF) binder was added to the ball-milled mixture, resulting in a final mass ratio of active material, C45 and PVDF of 70:22:8. In order to obtain the electrode slurry, an appropriate amount of N-methyl-2-pyrrolidone (NMP) solvent was added to the mixture and the slurry was uniformly coated on a carbon-coated Al foil followed by overnight drying in vacuum oven at 120 °C. The dried electrodes were calendered and punched into round disc electrodes with a 10 mm dia. cutter, and the active material of each disk was estimated as 3.0–4.0 mg cm^{-2}. For the electrochemical measurements, two-electrode Swagelok cells were used where sodium (99.9% Sigma–Aldrich, 99.9%) metal acts as the counter electrode. Three different electrolytes were used for testing, a) 1 M NaClO$_4$ in EC/PC/DMC (wt ratio as 4.5:4.5:1) with 3 wt% fluoroethylene carbonate (FEC) b) 1 M NaPF$_6$ in diglyme and c) 0.7 M NaBF$_4$ in diglyme. These electrolytes were denoted as "NaClO$_4$/carbonate," "NaPF$_6$/diglyme," and "NaBF$_4$/diglyme," respectively. The solvents were extensively dried on molecular sieves to capture the moisture.

The cells were assembled in an argon-filled glove box (MBraun; O$_2$ < 0.1 ppm and H$_2$O < 0.1 ppm) and galvanostatic charge/discharge tests were conducted using a battery cycler (BT-lab, Biologic) at different C-rates in the voltage window of 3.0–1.0 V versus Na$^+$/Na^0 or otherwise mentioned. Cyclic voltammetry (CV) was conducted at a scan rate of 0.05 mV s^{-1}. Galvanostatic intermittent titration technique (GITT) and potentiostatic intermittent titration technique (PITT) experiments were performed after the third cycle. GITT measurements consisted of 0.5 h of charges or discharges at C/10 rate followed by a rest of 2 h to obtain a steady state. PITT measurements were conducted using potential steps of 5 mV limited by a minimum current equivalent to a C/20 regime. Electrochemical impedance spectroscopy (EIS) was employed in the range of 100 kHz to 10 mHz, with the amplitude of the AC voltage set at 10 mV (Bio-Logic VSP-300). In situ XRD and ex situ XPS studies were carried out to examine the Na insertion/extraction mechanism. The sodium-ion full cells were fabricated using NVP as the cathode and N$_{1.5}$VNbP as the anode. The synthesis of NVP was carried out according to the literature.[57] The NVP electrode was prepared by mixing the active material, Super C45 and PVDF in a weight ratio of 70:22:8 with NMP and the slurry was coated on an Al foil. The capacity ratio between anode and cathode was maintained at ≈1.2:1 (mass ratio is ≈1.07:1), so that the cell capacity was limited by the cathode. Galvanostatic charge/discharge measurements on the full Na-ion cells were carried out in the window of 2.6–0.2 V.

In situ XRD: The in situ XRD measurements were performed in Bruker D8-diffractometer using a homemade in situ cell fitted with a Be-window, where the NASICON anode was coated on a pinhole-free thin aluminum foil (Alfa, 99.99%, 10 mm thickness) and placed below the Be-window. The XRD patterns were collected with an interval of 1 h at different states-of-charge upon cycling the cell at C/10 rate in the window of 3.0–1.0 V versus Na$^+$/Na^0.

XAS Measurements: The XAS measurements of pristine and cycled electrodes at different states-of-charge were carried out at PETRA-III beamline P65 at DESY in Hamburg. The XAS measurements at Nb and V K-edge were performed at room temperature in fluorescence mode and transmission mode, respectively, using gas ionization chambers to monitor the intensities of the incident and transmitted X-ray through a PIPS diode. The energy of Nb and V-K edge was calibrated by defining the inflection point (i.e., first derivative maxima) of Nb and V foil as 18 987.5 eV and 5465.1 eV respectively. The ex situ electrodes were sealed in between Kapton tapes inside the Ar-filled glove box and used directly for the data collection. All XAS data were collected at room temperature with a Si (111) double crystal monochromator and were processed using the DEMETER software package.[58,59]

Computational: All DFT calculations were performed in the Vienna Ab Initio Simulation Package (VASP),[60,61] which employed the frozen-core project augmented wave potentials (PAW)[62] to describe the core electrons, and a 520 eV kinetic energy cutoff for expanding the plane wave basis set was utilized. The strongly constrained and appropriately normed (SCAN)[63] functional was used, with a Hubbard U[64–67] correction (i.e., SCAN+U) of 1.0 eV to remove the spurious self-interaction of the Vanadium d electrons. The irreducible Brillouin zone using was sampled a 4 × 4 × 4 Γ-centered k-point mesh (corresponding to a minimum mesh density of 32 k-points per Å). The convergence criteria for the calculations were set as 0.01 meV and |0.03| eV Å^{-1} for the total energies and atomic forces, respectively. The lattice vectors, cell shapes, and cell volumes were relaxed without keeping any underlying symmetry.

To generate derivative structures with different Na-vacancy configurations, the structure of NVP was taken from the inorganic crystal structure database,[68] and a primitive structure was generated (with 2 V$_2$(PO$_4$)$_3$ formula units)[69] to reduce computational effort. Subsequently, 3 out of the 4 V sites were substituted in the NVP primitive cell, and considered the occupation of three out of eight possible Na sites (i.e., include Na(1) and Na(2) sites), corresponding to a Na-content of x = 1.5 in Na$_x$V$_{0.5}$Nb$_{1.5}$(PO$_4$)$_3$. Thus, all possible Na-vacancy orderings and all possible Nb-V orderings corresponding to the composition of Na$_{1.5}$V$_{0.5}$Nb$_{1.5}$(PO$_4$)$_3$, using the pymatgen[70] package were enumerated, resulting in a set of 20 symmetrically distinct configurations and subsequently used DFT to identify the ground state configuration. Further, the same Nb-V ordering as in the ground state of Na$_{1.5}$V$_{0.5}$Nb$_{1.5}$(PO$_4$)$_3$ and only enumerated the Na-vacancy configurations at all the ﹨ Na-compositions (i.e., from x = 0 to 4 in Na$_x$V$_{0.5}$Nb$_{1.5}$(PO$_4$)$_3$) was used. This is because, the experimentally synthesized composition in this work was Na$_{1.5}$V$_{0.5}$Nb$_{1.5}$(PO$_4$)$_3$ and it did not expect significant transition metal migration as Na is exchanged within the NASICON structure—hence, the V-Nb configuration from the as-synthesized sample should not change significantly with Na-content change. Once the ground state Na-vacancy orderings across all Na-compositions were obtained, the 0 K convex hull was constructed and calculated the Na-intercalation voltage profile, using methods described in previous studies.[71,72]

Supporting Information

Supporting Information is available from the Wiley Online Library or from the author.

Acknowledgements

Conflict of Interest

The authors declare no conflict of interest.

Data Availability Statement

The data that support the findings of this study are available from the corresponding author upon reasonable request.

Keywords

[1] D. Larcher, J.-M. Tarascon, *Nat. Chem.* **2015**, *7*, 19.
[2] C. Vaalma, D. Buchholz, M. Weil, S. Passerini, *Nat. Rev. Mater.* **2018**, *3*, 18013.
[3] T. Hosaka, K. Kubota, A. S. Hameed, S. Komaba, *Chem. Rev.* **2020**, *120*, 6358.
[4] Y. Tian, G. Zeng, A. Rutt, T. Shi, H. Kim, J. Wang, J. Koettgen, Y. Sun, B. Ouyang, T. Chen, Z. Lun, Z. Rong, K. Persson, G. Ceder, *Chem. Rev.* **2021**, *121*, 1623.
[5] T. Liu, Y. Zhang, Z. Jiang, X. Zeng, J. Ji, Z. Li, X. Gao, M. Sun, Z. Lin, M. Ling, J. Zheng, C. Liang, *Energy Environ. Sci.* **2019**, *12*, 1512.
[6] J. Y. Hwang, S. T. Myung, Y. K. Sun, *Chem. Soc. Rev.* **2017**, *46*, 3529.
[7] K. Chayambuka, G. Mulder, D. L. Danilov, P. H. L. Notten, *Adv. Energy Mater.* **2018**, *8*, 1800079.
[8] P. K. Nayak, L. Yang, W. Brehm, P. Adelhelm, *Angew. Chem. Int. Ed.* **2018**, *57*, 102.
[9] M. Lao, Y. Zhang, W. Luo, Q. Yan, W. Sun, S. X. Dou, *Adv. Mater.* **2017**, *29*, 1700622.
[10] H. Tan, D. Chen, X. Rui, Y. Yu, *Adv. Funct. Mater.* **2019**, *29*, 1808745.
[11] E. Irisarri, A. Ponrouch, M. R. Palacin, *J. Electrochem. Soc.* **2015**, *162*, A2476.
[12] Z. Li, Z. Jian, X. Wang, I. A. Rodríguez-Pérez, C. Bommier, X. Ji, *Chem. Commun.* **2017**, *53*, 2610.
[13] A. Rudola, K. Saravanan, C. W. Mason, P. Balaya, *J. Mater. Chem. A* **2013**, *1*, 2653.
[14] P. Senguttuvan, G. Rousse, V. Seznec, J.-M. Tarascon, M. R. Palacín, *Chem. Mater.* **2011**, *23*, 4109.
[15] T. Jin, H. Li, K. Zhu, P. F. Wang, P. Liu, L. Jiao, *Chem. Soc. Rev.* **2020**, *49*, 2342.
[16] D. Deb, G. Sai Gautam, *J. Mater. Res.* **2022**, *37*, 3169.
[17] C. Delmas, F. Cherkaoui, A. Nadiri, P. Hagenmuller, *Mater. Res. Bull.* **1987**, *22*, 631.
[18] P. Senguttuvan, G. Rousse, M. E. Arroyo Y De Dompablo, H. Vezin, J. M. Tarascon, M. R. Palacín, *J. Am. Chem. Soc.* **2013**, *135*, 3897.
[19] Y. Fang, L. Xiao, J. Qian, Y. Cao, X. Ai, Y. Huang, H. Yang, *Adv. Energy Mater.* **2016**, *6*, 1502197.
[20] J. Yang, H. Wang, P. Hu, J. Qi, L. Guo, L. Wang, *Small* **2015**, *11*, 3744.
[21] W. Wu, J. Yan, A. Wise, A. Rutt, J. F. Whitacre, *J. Electrochem. Soc.* **2014**, *161*, A561.
[22] T. Akçay, M. Häringer, K. Pfeifer, J. Anhalt, J. R. Binder, S. Dsoke, D. Kramer, R. Mönig, *ACS Appl. Energy Mater.* **2021**, *4*, 12688.
[23] Z. Jian, Y. Sun, X. Ji, *Chem. Commun.* **2015**, *51*, 6381.
[24] Z. Jian, L. Zhao, H. Pan, Y. S. Hu, H. Li, W. Chen, L. Chen, *Electrochem. Commun.* **2012**, *14*, 86.
[25] B. Patra, K. Kumar, D. Deb, S. Ghosh, G. S. Gautam, P. Senguttuvan, *J. Mater. Chem. A* **2023**, *11*, 8173.
[26] P. Hohenberg, W. Kohn, *Phys. Rev.* **1964**, *136*, B864.
[27] W. Kohn, L. J. Sham, *Phys. Rev.* **1965**, *140*, A1133.
[28] S. Li, Y. Dong, L. Xu, X. Xu, L. He, L. Mai, *Adv. Mater.* **2014**, *26*, 3545.
[29] Y. Zhang, H. Zhao, Y. Du, *J. Mater. Chem. A* **2016**, *4*, 7155.
[30] W. Ren, Z. Zheng, C. Xu, C. Niu, Q. Wei, Q. An, K. Zhao, M. Yan, M. Qin, L. Mai, *Nano Energy* **2016**, *25*, 145.
[31] D. Wang, X. Bie, Q. Fu, D. Dixon, N. Bramnik, Y.-S. Hu, F. Fauth, Y. Wei, H. Ehrenberg, G. Chen, F. Du, *Nat. Commun.* **2017**, *8*, 15888.
[32] Y. Liu, X. Rong, R. Bai, R. Xiao, C. Xu, C. Zhang, J. Xu, W. Yin, Q. Zhang, X. Liang, Y. Lu, J. Zhao, L. Chen, Y.-S. Hu, *Nat. Energy* **2023**, *8*, 1088.
[33] R. Liu, G. Xu, Q. Li, S. Zheng, G. Zheng, Z. Gong, Y. Li, E. Kruskop, R. Fu, Z. Chen, K. Amine, Y. Yang, *ACS Appl. Mater. Interfaces* **2017**, *9*, 43632.
[34] S. Park, J.-N. Chotard, D. Carlier, F. Fauth, A. Iadecola, C. Masquelier, L. Croguennec, *Chem. Mater.* **2023**, *35*, 3181.
[35] S. Park, J.-N. Chotard, D. Carlier, I. Moog, F. Fauth, A. Iadecola, L. Croguennec, C. Masquelier, *Chem. Mater.* **2022**, *34*, 4142.
[36] N. R. Khasanova, R. V. Panin, I. R. Cherkashchenko, M. V. Zakharkin, D. A. Novichkov, E. V. Antipov, *ACS Appl. Mater. Interfaces* **2023**, *15*, 30272.
[37] S. Patoux, G. Rousse, J. Leriche, C. Masquelier, *Chem. Mater.* **2003**, *15*, 2084.
[38] J. R. Kim, G. G. Amatucci, *Chem. Mater.* **2015**, *27*, 2546.
[39] G. S. Gautam, P. Canepa, *Magnesium Batteries: Research and Applications*, The Royal Society Of Chemistry, London, UK **2019**, p. 79.
[40] H. Kim, J. Hong, Y. U. Park, J. Kim, I. Hwang, K. Kang, *Adv. Funct. Mater.* **2015**, *25*, 534.
[41] K. Li, J. Zhang, D. Lin, D.-W. Wang, B. Li, W. Lv, S. Sun, Y.-B. He, F. Kang, Q.-H. Yang, L. Zhou, T.-Y. Zhang, *Nat. Commun.* **2019**, *10*, 725.
[42] B. Zhang, G. Rousse, D. Foix, R. Dugas, D. A. D. Corte, J.-M. Tarascon, *Adv. Mater.* **2016**, *28*, 9824.
[43] C. Wang, L. Wang, F. Li, F. Cheng, J. Chen, *Adv. Mater.* **2017**, *29*, 1702212.
[44] M. Galceran, J. Rikarte, M. Zarrabeitia, M. C. Pujol, M. Aguiló, M. Casas-Cabanas, *ACS Appl. Energy Mater.* **2019**, *2*, 1923.
[45] R. I. R. Blyth, H. Buqa, F. P. Netzer, M. G. Ramsey, J. O. Besenhard, P. Golob, M. Winter, *Appl. Surf. Sci.* **2000**, *167*, 99.
[46] M. A. Muñoz-Márquez, M. Zarrabeitia, E. Castillo-Martínez, A. Eguía-Barrio, T. Rojo, M. Casas-Cabanas, *ACS Appl. Mater. Interfaces* **2015**, *7*, 7801.
[47] J. Zhang, D. W. Wang, W. Lv, S. Zhang, Q. Liang, D. Zheng, F. Kang, Q. H. Yang, *Energy Environ. Sci.* **2017**, *10*, 370.
[48] X. Bi, X. Ren, Z. Huang, M. Yu, E. Kreidler, Y. Wu, *Chem. Commun.* **2015**, *51*, 7665.
[49] M. Dahbi, N. Yabuuchi, M. Fukunishi, K. Kubota, K. Chihara, K. Tokiwa, X. F. Yu, H. Ushiyama, K. Yamashita, J. Y. Son, Y. T. Cui, H. Oji, S. Komaba, *Chem. Mater.* **2016**, *28*, 1625.
[50] G. G. Eshetu, T. Diemant, M. Hekmatfar, S. Grugeon, R. J. Behm, S. Laruelle, M. Armand, S. Passerini, *Nano Energy* **2019**, *55*, 327.
[51] D. Su, K. Kretschmer, G. Wang, *Adv. Energy Mater.* **2016**, *6*, 1501785.
[52] M. Guin, F. Tietz, *J. Power Sources* **2015**, *273*, 1056.

[53] Z. Zhang, Z. Zou, K. Kaup, R. Xiao, S. Shi, M. Avdeev, Y. Hu, D. Wang, B. He, H. Li, X. Huang, L. F. Nazar, L. Chen, *Adv. Energy Mater.* **2019**, *9*, 1902373.

[54] Z. Deng, T. P. Mishra, E. Mahayoni, Q. Ma, A. J. K. Tieu, O. Guillon, J.-N. Chotard, V. Seznec, A. K. Cheetham, C. Masquelier, G. S. Gautam, P. Canepa, *Nat. Commun.* **2022**, *13*, 4470.

[55] J. Rodríguez-Carvajal, *Phys. B Condens. Matter* **1993**, *192*, 55.

[56] H. M. Rietveld, *J. Appl. Crystallogr.* **1969**, *2*, 65.

[57] S. Ghosh, N. Barman, B. Patra, P. Senguttuvan, *Adv. Energy Sustain. Res.* **2022**, *3*, 2200081.

[58] M. Newville, *J. Synchrotron. Radiat.* **2001**, *8*, 322.

[59] B. Ravel, M. Newville, *J. Synchrotron. Radiat.* **2005**, *12*, 537.

[60] G. Kresse, J. Furthmüller, *Phys. Rev. B* **1996**, *54*, 11169.

[61] G. Kresse, J. Hafner, *Phys. Rev. B* **1993**, *47*, 558.

[62] G. Kresse, D. Joubert, *Phys. Rev. B Condens. Matter Mater. Phys.* **1999**, *59*, 1758.

[63] J. Sun, A. Ruzsinszky, J. Perdew, *Phys. Rev. Lett.* **2015**, *115*, 036402.

[64] G. Sai Gautam, E. A. Carter, *Phys. Rev. Mater.* **2018**, *2*, 095401.

[65] V. I. Anisimov, J. Zaanen, O. K. Andersen, *Phys. Rev. B* **1991**, *44*, 943.

[66] S. Swathilakshmi, R. Devi, G. Sai Gautam, *J. Chem. Theory Comput.* **2023**, *19*, 4202.

[67] S. Dudarev, G. Botton, *Phys. Rev. B Condens. Matter Mater. Phys.* **1998**, *57*, 1505.

[68] M. Hellenbrandt, *Crystallogr. Rev.* **2004**, *10*, 17.

[69] D. B. Tekliye, A. Kumar, X. Weihang, T. D. Mercy, P. Canepa, G. Sai Gautam, *Chem. Mater.* **2022**, *34*, 10133.

[70] S. P. Ong, W. D. Richards, A. Jain, G. Hautier, M. Kocher, S. Cholia, D. Gunter, V. L. Chevrier, K. A. Persson, G. Ceder, *Comput. Mater. Sci.* **2013**, *68*, 314.

[71] B. Singh, Z. Wang, S. Park, G. S. Gautam, J. N. Chotard, L. Croguennec, D. Carlier, A. K. Cheetham, C. Masquelier, P. Canepa, *J. Mater. Chem. A* **2021**, *9*, 281.

[72] Z. Wang, S. Park, Z. Deng, D. Carlier, J. N. Chotard, L. Croguennec, G. S. Gautam, A. K. Cheetham, C. Masquelier, P. Canepa, *J. Mater. Chem. A* **2022**, *10*, 209.